ISSN 1995-0780, Nanotechnologies in Russia, 2018, Vol. 13, Nos. 1–2, pp. 76–83. © Pleiades Publishing, Ltd., 2018.
Original Russian Text © A.A. Sivkov, A.S. Ivashutenko, I.A. Rakhmatullin, Yu.L. Shanenkova, A.I. Zimmermann, 2018, published in Rossiiskie Nanotekhnologii, 2018, Vol. 13, Nos. 1–2.

Study of the Phase Composition and Structure of the Nanodispersed Al–O Powder Produced by a Plasmodynamic Method

A. A. Sivkov[a], A. S. Ivashutenko[a], I. A. Rakhmatullin[a], Yu. L. Shanenkova[a]*, and A. I. Zimmermann[a]

[a] *Tomsk Polytechnic University, Tomsk, 634050 Russia*

**e-mail: julia_kolganova@mail.ru*

Received December 12, 2017; in final form, February 20, 2018

Abstract—In this work we report the results of experimental studies of the phase composition and structure of the nanodispersed Al–O powder produced by the plasmodynamic method. Using X-ray diffractometry and transmission electron microscopy, we show that the product contains σ-Al_2O_3 and $MgAl_2O_4$. The phase composition evolution of the initial product of plasmodynamic synthesis is studied during its heat treatment. Thermogravimetric analysis in an argon atmosphere shows no changes in mass of the sample weighed when it is heated, while differential scanning calorimetry studies indicate a marked manifestation of the endothermic effect.

DOI: 10.1134/S1995078018010135

INTRODUCTION

Aluminum oxide in the nanostructured state due to a unique set of its properties (high mechanical strength, wear resistance, fire resistance, hardness, chemical and radiation resistance, high electric resistivity, and high specific heat) is widely used in various fields of science, medicine, and technology [1–5]. The presence of a large number of crystalline modifications (α, σ, γ, δ, χ, θ, etc.) in aluminum oxide is known to determine its wide application and the possibility of using it as an adsorbent, catalyst, and abrasive [6]; in ceramic products of structural and biomedical applications; and for the manufacture of refractory products [7]. Porous alumina can be used in the development of environmental sensors (humidity sensors) and as a template for the production of fibrillar nanoparticles with magnetic properties [8, 9].

At present, nanomaterials based on the aluminum–oxygen system are mostly produced by the gas-phase method [1], the electric explosion of conductors [10], sol-gel [11], or laser [12] methods. Each of these methods has its own peculiarities. For example, the gas-phase method is considered relatively simple with the ability to regulate the particle size, while the sol-gel method is distinguished by a high purity of the products. Meanwhile, the main advantage of the plasmochemical method is its high productivity. At the same time, the sol-gel method is characterized by the complexity of the equipment used and its high cost. When the material is obtained by the plasmochemical method, the probability of product contamination increases (a large number of impurities) and the particle size distribution increases. In general, all known methods for producing nanodispersed products based on aluminum are complex and multistage.

To overcome the shortcomings mentioned above [13, 14], a new method of plasma-dynamic synthesis (PDS) using a pulsed high-current coaxial magnetoplasma accelerator (CMPA) of an erosion type was developed at Tomsk Polytechnic University. The main advantages of this method are as follows: its rate, the simplicity of obtaining the material, one-stage production, and the possibility of synthesizing rare crystalline modifications. In the considered design version of the plasma accelerator (see the EXPERIMENTAL section), the product synthesis is carried out for 1 ms and the main consumables do not require any additional preliminary preparation. Also, in comparison with the chemical methods of obtaining alumina phases, the proposed method allows one to obtain up to 20 g of product in one cycle of accelerator work.

EXPERIMENTAL

In this paper we present the results of experimental research on direct plasmodynamic synthesis to produce highly disperse alumina. The central electrode of the accelerator was made in the form of an aluminum stud with a diameter of 12 mm. The channel electrode was made in the form of an aluminum pipe with a length of 200 mm and an outer diameter of 20 mm and

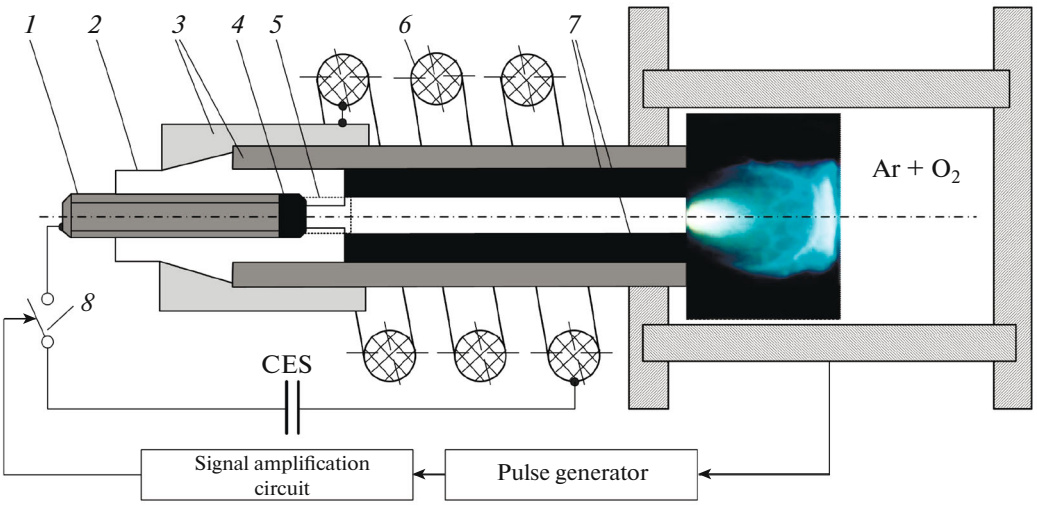

Fig. 1. (Color online) Scheme of the setup based on CMPA: (*1*) central electrode, (*2*) insulator, (*3*) metal case, (*4*) aluminum tip, (*5*) channel for the formation of the plasma structure, (*6*) inductor, (*7*) aluminum accelerator channel of the barrel, and (*8*) power switches; CES is capacitive energy storage.

an internal diameter of the accelerating channel of 16 mm.

The major metallic precursor, aluminum, is produced by electroerosion from the cylindrical surface of the accelerator channel (AC). Captured by the plasma structure of the accelerated high-current discharge under high-temperature conditions (~10^4 K), it transforms into the plasma state. Then, aluminum is taken out of AC at a velocity of ~10^3 m/s and enters the hermetic volume of the reactor chamber (RC), which is filled with the gaseous precursor, oxygen, and argon in a ratio of 80 to 20%, respectively. In AC, the plasmochemical synthesis of materials occurs, followed by their sputtering in the liquid phase at the front of the head jet of an electric discharge plasma and crystallization with the formation of highly disperse crystalline phase particles (Fig. 1). The entire process is of a pulsed nature with a wide range of changes in temperature, pressure, velocity of plasma-jet outflow, and spraying of the synthesized material.

The power supply of the accelerator consisted of a pulsed power source with a capacitor bank capacity of $C = 14.4$ mF at a charging voltage of $U_{sar} = 2.1$ kV and an inductance of a low-resistance discharge circuit of $L = 1.5 \times 10^{-6}$ H. With such parameters of the system, the power supply was experimentally established to ensure stable operation of the accelerator in five consecutive experiments [15].

Figure 2 shows oscillograms of the current pulse $I(t)$ and the voltage at the electrodes of the accelerator $U(t)$, as well as the calculated curves of the $P(t)$ electric power of the discharge in AC and the supplied energy $W(t)$.

Cylindrical CR was filled with a mixture of argon and oxygen at atmospheric pressure and room temperature. Postexperimentation of CR was performed after the complete precipitation of the highly disperse product from its suspended state. The white powder was collected from the CR walls and analyzed without any sample preparation.

X-ray phase analysis was performed using a Shimadzu XRD 7000S (CuK_α-radiation) diffractometer with a Shimadzu CM 3121 monochromator. The scanning electron analysis was performed using a Hitachi TM-3000 microscope. Transmitting electron microscopy (TEM) was carried out using a Philips CM12 microscope with a charging voltage of up to 100 kV. Thermogravimetry (TG) and differential scanning calorimetry (DSC) are performed using a thermoanalytical system for constructing synchronous characteristics of DSC/TG STA 449 F3 Jupiter.

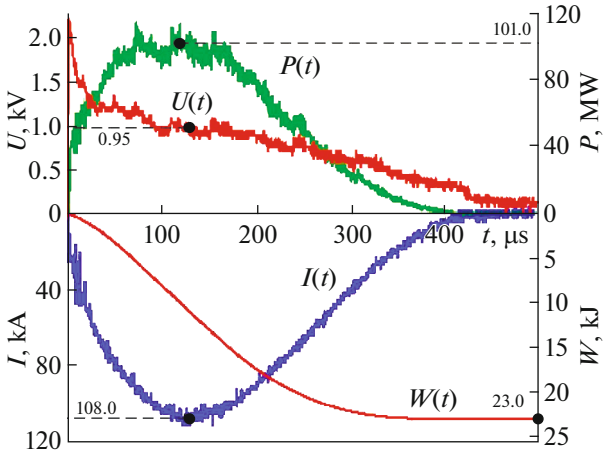

Fig. 2. (Color online) Oscillograms of current, voltage, power, and energy of the product synthesis process.

RESULTS AND DISCUSSION

In the series of experimental studies, at 80% of O_2 in the gas mixture with Ar, the possibility of igniting the accelerator channel was found to be completely eliminated and the absence of crystalline aluminum in the finely dispersed fraction of the synthesized product is ensured. This is evidenced by the X-ray diffraction pattern (XRD pattern) shown in Fig. 3. According to the presented data, in addition to reflections of the main material of the Al–O system, the reflexes of magnesium spinel $MgAl_2O_4$ are present in the XRD angular spectrum. Its "appearance" is due to the use of an aluminum alloy with a 7.5%-magnesium content as the accelerator channel of CMPA. The high intensity of coherent reflexes presented in the XRD-spectrum indicates the domination of the crystalline component in the product with a volume content of ~88%. The diffuse halo with a maximum at $2\theta \approx 35.0°$ indicates the presence of an X-ray amorphous component with an estimated content of ~12%.

Accounting for the known elemental composition of the main metal precursor with aluminum as a major component, the main crystalline phase of the PDS product can be assumed to be nonstoichiometric and metastable alumina, which is closest to the structural model of σ-$Al_{2.667}O_4$ with the cubic syngony of the spatial group Fd-3m (227) with the period of the crystal lattice a = 7.9480 Å (number in PDF-2: 80-1385). However, the maxima of all diffraction reflections in the XRD spectrum of the PDS product (Fig. 3) are shifted to the left in the direction of a decrease of 2θ by approximately 0.06° relative to the maxima of the adopted structural model and are distinguished by some asymmetry. These deviations are practically eliminated by taking into account the formation of the second crystalline spinel phase. In view of the above, the structural model of $MgAl_2O_4$ spinel (card no. 072-6955) with the cubic syngony of the spatial group Fd-3m with the lattice period a = 7.96121 Å is most acceptable. The presence of a diffuse halo in the XRD picture above indicates the presence of other metastable phases in the X-ray amorphous state in the X-ray diffraction pattern, whose lines are at the level of background oscillations, such as orthorhombic modification or an indefinite monoclinic modification of Al–Mg–O (10-238). Of particular note is the complete absence in the XRD picture of the initial product of the PBC reflections corresponding to the stable crystalline phase of α-Al_2O_3 and the phase of pure metallic aluminum.

Figure 4 shows a transmission electron microscopy (TEM) image of the PDS product. In the light-field TEM image of a typical particles cluster, most particles are seen to belong to a nanoscale fraction with a size distribution from ~10 to ~200 nm. However, in the powder there is a small number of particles in the submicron range of sizes. One characteristic feature of the powder is that it consists of two morphological

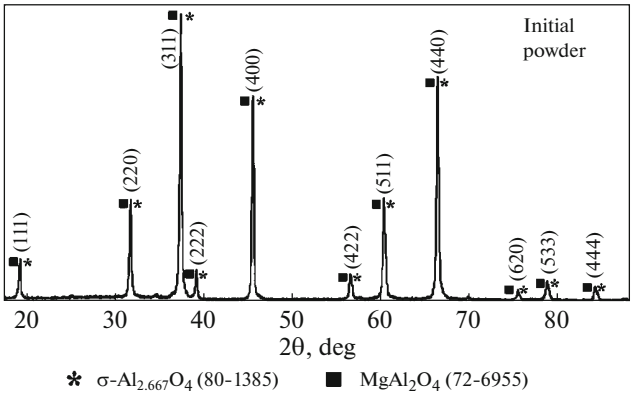

Fig. 3. XRD image of the PDS product.

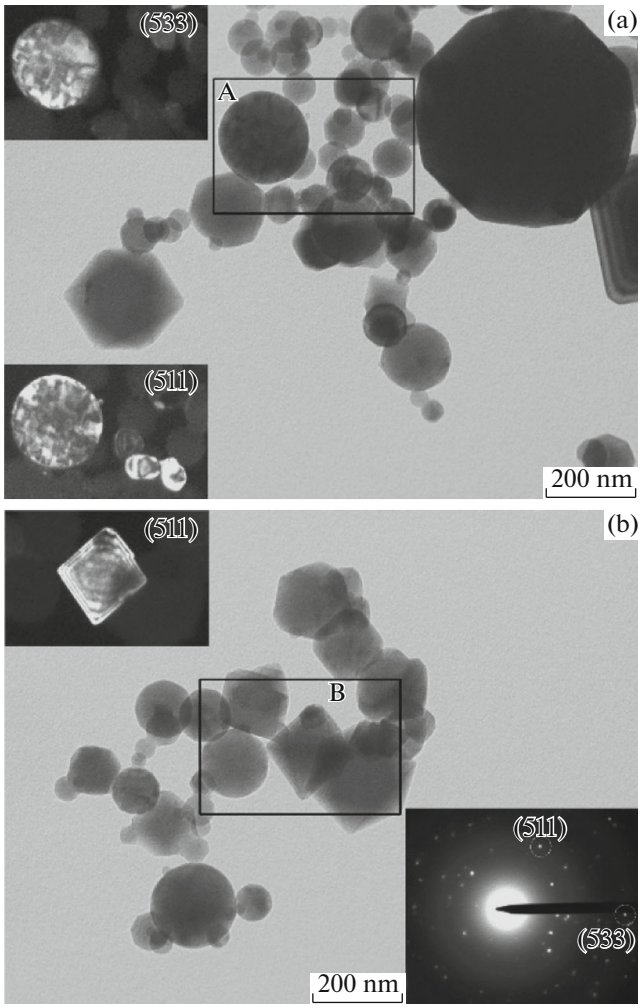

Fig. 4. TEM images of the PDS product: (a) cluster no. 1 and (b) cluster no. 2.

types of objects: spherical particles and particles with a proper crystalline form mostly of a cubic shape that are located in the sample at different angles relative to the main electron beam. In the individual particles,

sharp diffraction contours of the extinction of planes packets located at Bragg angles to the electron beam are seen. These phenomena unambiguously confirm the single-crystal structure of the particles. The structure analysis of aluminum oxides produced by other known methods indicates basically the spherical structure of the particles [1, 16]. This kind of object is specific of the α-phase, σ-phase, and γ-phase of aluminum oxide and it agrees completely with the results obtained in this work. The second isolated form of particles in the synthesized product (rhombus) is an unusual phenomenon for a given type of material. This is easily explained by the cubic structure of the phase.

In the picture of electron microdiffraction in the selected area (SAED), the reflections of the cubic phases of σ-$Al_{2.667}O_4$ and $MgAl_2O_4$ pertaining to one spatial group Fd-3m are identified only. In Table 1, for comparison, the values of the interplanar spacing *d* for the main crystallographic directions of the structural models under consideration and the *d* values determined in SAED and XRD with indications of Miller indices are given. It is seen that, within the accuracy of phase microanalysis, the d values determined by SAED can correspond to both structural models. This circumstance makes it difficult to uniquely identify the morphological type of particles of a particular phase composition. For example, in the dark-field TEM images of a typical spherical particle A shown in Fig. 4, bright contour glows of plane packets of several different nanocrystallites in a spherical particle are observed under the light of diffracted electron beams on planes in directions [533] and [511] with interplanar distances of 1.2129 and 1.5289 Å, respectively, determined according to SAED. These values of the interplanar distances can correspond to

Table 1. Interplanar distances and Miller indices

Interplanar distances *d*, Å				Miller indices
XRD	SAED	σ-$Al_{2.667}O_4$ (80-1385)	$MgAl_2O_4$ (72-6955)	
4.6093	4.5720	4.5888	4.5964	111
2.8160	2.8100	2.8100	2.8147	220
2.4007	2.4059	2.3964	2.4004	311
2.2974	2.2969	2.2944	2.2982	222
1.9898	1.9850	1.9870	1.9903	400
1.6242	1.6205	1.6224	1.6250	422
1.5309	1.5289	1.5296	1.5321	511
1.4060	1.4076	1.4050	1.4073	440
1.2132	1.2129	1.1982	1.2002	533

both the phase of σ-$Al_{2.667}O_4$ with d_{533} = 1.1982 nm and d_{511} = 1.5296 nm and the spinel phase of $MgAl_2O_4$ d_{533} = 1.2002 nm and d_{511} = 1.5321 nm due to their close arrangement of the reflexes. In the dark-field image, strictly ordered contours of the plane packets in a geometrically correct, cubic-shape particle B can be interpreted in a similar way, since the particle can represent both the metastable phase of aluminum oxide and the spinel phase.

Based on the TEM data, we can only conclude that absolutely spherical particles are polycrystalline nanoscale or submicron aggregates that are formed from the liquid phase. The particles of the second morphological type B are monocrystallites of one of the phases under consideration as evidenced by their morphology of the simplest forms of growth of cubic-

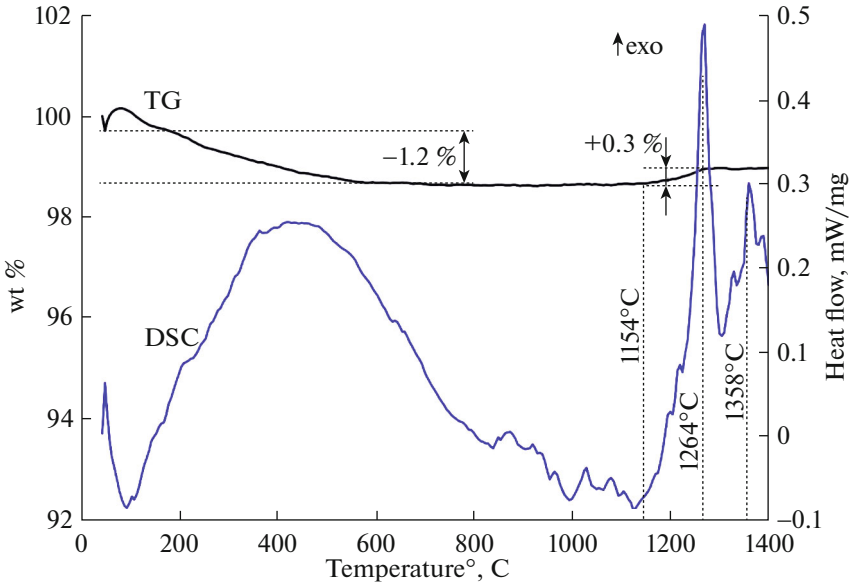

Fig. 5. (Color online) Thermogravimetry and differential scanning calorimetry.

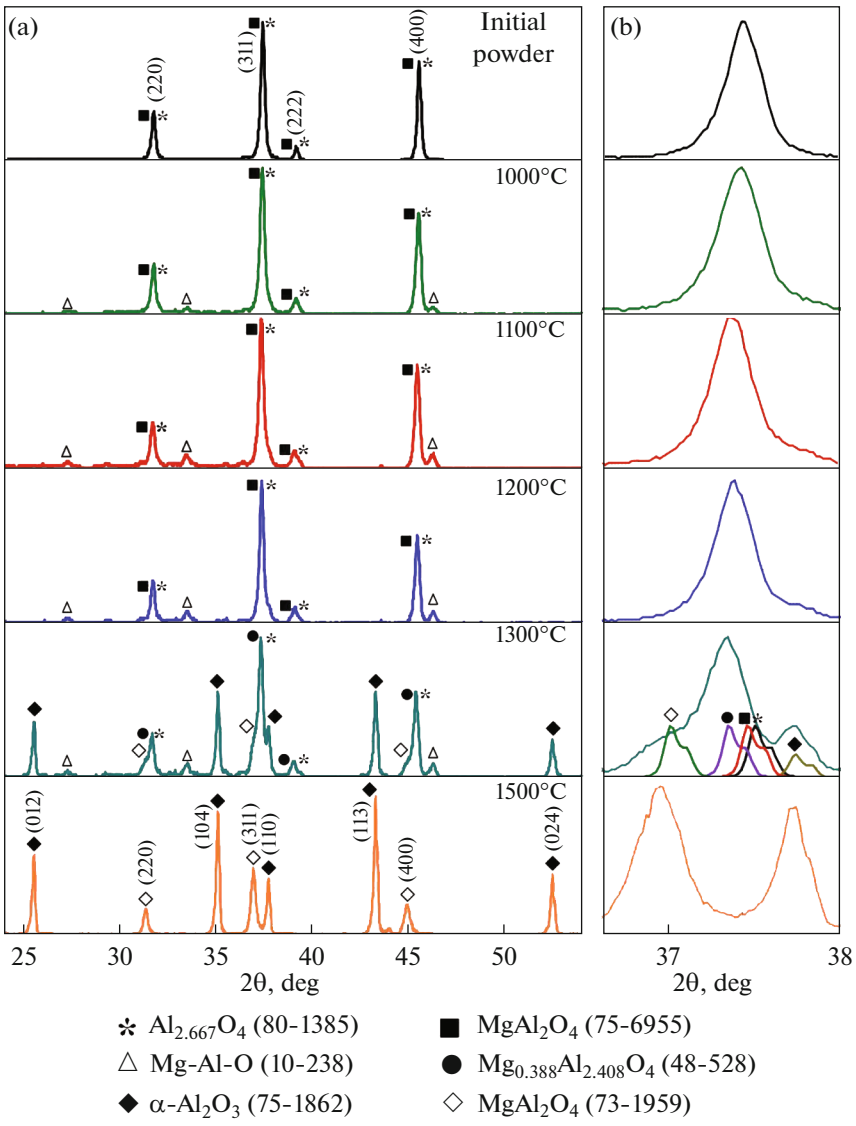

Fig. 6. (Color online) X-ray phase analysis of the PDS product in the temperature range: (a) the complete form of the XRD patterns and (b) XRD image of the isolated main reflex of the α-Al_2O_3 phase.

shape crystals and the observed regular extinction contours that, in general, reproduce the shape of the reflecting planes of a single crystal at its position at the Bragg angle relative to the main electron beam.

The next stage was investigating how the phase composition of the initial PDS product evolved during its thermal treatment. Thermogravimetric analysis in an argon atmosphere showed no changes in the mass of the sample weighed when it was heated to 1200°C at a rate of 40°C/min. However, starting at ~1100°C, differential scanning calorimetry studies showed a noticeable manifestation of the endothermic effect due to the onset of phase transition processes in the system under consideration in accordance with the known concepts [17].

As is shown in Fig. 5, the TG and DSC curves obtained while the powder was heated in air show more noticeable changes in the state of the PDS product. At the initial stage in the temperature range of up to ~800°C, the powder mass decreases smoothly by ~1.5% due mainly to the removal of moisture and adsorbed gases. When the temperature reaches 1154°C, an intensive exothermic process (DSC curve) begins and is accompanied by a gradual increase in mass by 0.3% to 1300°C. In this temperature range, the superoxidation of nonstoichiometric compounds of aluminum oxides and spinel and more inertial phase-transition processes are likely superimposed. The subsequent peak on the DSC curve at 1358°C against a background of unchanged mass corresponds definitely to a more intense transition of the metastable phases into a thermodynamically stable state.

Taking into account the TG and DSC data, experiments on the thermal treatment of the PBC product in air were carried out at a temperature growth rate of 10°C/min and isothermal aging for 30 min at 850, 1000, 1100, 1200, 1300, and 1500°C, followed by natural cooling to room temperature. Figure 6 shows fragments of XRD patterns in the most representative range of 2θ of the initial product and powders after annealing at the temperatures specified above, except for 850°C, since there are practically no changes in comparison with the initial product below 850°C.

Noticeable changes appear in XRD images of the powders after annealing at 1000°C or higher. They show weak broad reflexes over the entire range of 2θ (from 20° to 70°) and become especially noticeable in the vicinity of angles of 33.5°, 36.5°, 46.4°, and 67.1°. The intensities of these reflections increase with an annealing temperature of 1200°C (Fig. 6). These reflections most likely correspond to an undefined (monoclinic) modification of the Mg–Al–O system, while the assumption on its presence in the X-ray amorphous state in the initial powder is stated above. This assumption agrees with the appearance of oscillations on the DSC curve (Fig. 5) in the temperature range from ~840 to 1100°C caused by the onset of recrystallization of this modification with the growth of its nanocrystallites. However, the reflections of this phase completely disappear in the XRD image after annealing at 1500°C, which also corresponds to the thermography data in connection with the continuation of the phase transformation with a temperature increase higher than ~1300°C.

All the diffractograms (Fig. 6) of powders annealed at 1000–1300°C show a consecutive displacement to the left of the 2θ maxima of the main reflections, in particular, the strongest maximum that is located at $2\theta = 37.4°$ for the initial product. For powders annealed at 1000–1200°C, this displacement does not exceed ~0.06°, which is within the accuracy of the diffractometer. For a powder after annealing at 1300°C, the displacement exceeds ~0.1°, and this should be considered evidence for a change in the structural parameters. The PDF-2 analysis showed that there are no structural models of aluminum oxides that could describe this change. Therefore, it should be associated with the structural changes of spinel and be taken as the closest model of the nonstoichiometric spinel $Mg_{0.388}Al_{2.408}O_4$ (card no. 48-528) with an increased cubic lattice parameter of $a = 7.9709$ Å (against $a = 7.9612$ Å for the starting material). Thus, the evolution with a successive increase in the annealing temperature up to 1300°C results mainly in the appearance and strengthening of the asymmetry of the bases of the main reflections in XRD patterns (Fig. 6) up to the appearance of pronounced maxima corresponding to both the gradual development of phase transitions with the formation of stable phases of corundum and spinel and reducing the intensity of intermediate modifications. This process is illustrated by the reflexes of

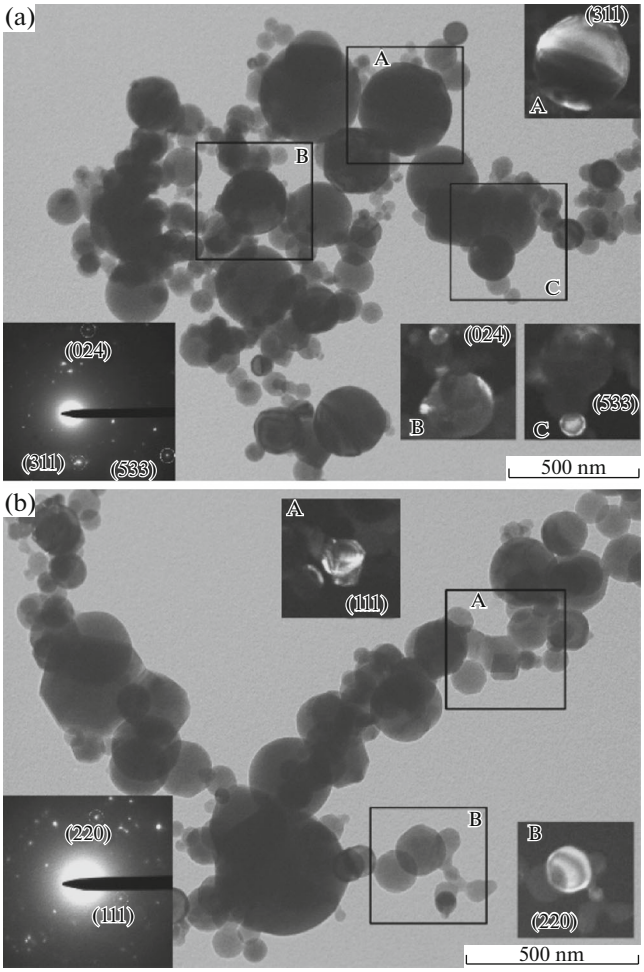

Fig. 7. TEM images of the material annealed at 1300°C: (a) cluster no. 1 and (b) cluster no. 2.

the structural models used against the background of the strongest reflex in the XRD image of the powder after annealing at 1300°C. The completion of phase transitions takes place during the annealing process at 1500°C, after which the phase composition of the powder becomes stable and most accurately corresponds to the composition of α-Al_2O_3 (card no. 75-1862) and $MgAl_2O_4$ (card no. 73-1959).

Figure 7 shows the transmission electron microscopy data of the powder after annealing in air at 1300°C. A comparison of the initial synthesized product shown in Fig. 4 with the TEM images indicates a significant increase in a particle size to 500 nm after heat treatment. All dark-field TEM images, in particular those under the light of the diffracted beams marked on SAED (Fig. 7), demonstrate the practical absence in the powder of spherical objects with a polycrystalline nanostructure that is specific of the original powder. This is quite an expected result due to the advantage of phase transformations and recrystallization in nanostructured systems.

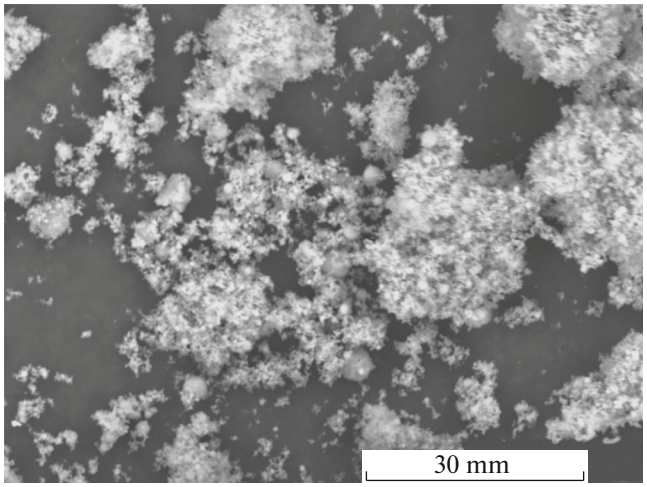

Fig. 8. SEM image of the powder after machining.

However, in most cases, phase microanalysis does not make it possible to identify the morphology of particles and the phase composition due to belonging to one spatial group Fd-3m and the proximity of the crystal structure parameters of all phases excepting corundum.

The dark-field image of the particle containing the formed corundum (α-Al_2O_3) was obtained under the light of the diffracted beam on the (024) planes (fragment B in Fig. 7a). The corresponding reflex in the XRD pattern has a maximum of $2\theta = 52.5°$ and is far from the reflexes of the other phases. In this picture, only the portion of the peripheral part of the 300-nm coarse particle is shining, as are several smaller objects.

An analysis of SEM images of powders annealed at 1500°C (Fig. 8) revealed the presence in the structure of the formation of loose specks that are easily destroyed during machining. The resulting biphasic powder has a wide size distribution from several tens of nanometers to about a micron. This will be a favorable factor for producing high-density ceramics.

Thus, the highly disperse PDS product with a bulk density after annealing in air was established to undergo structural transitions at higher temperatures, up to 1500°C, in contrast to known data indicating that thermodynamically stable corundum and spinel phases are formed at ~1100°C [18].

CONCLUSIONS

The possibility of producing a highly dispersed composite material consisting of two crystalline cubic phases, metastable alumina and spinel, is demonstrated using the plasmodynamic method. The major crystalline phase of the PDS product is established to be nonstoichiometric and metastable alumina, which is closest to the structural model of σ-$Al_{2.667}O_4$, as well as the structural model of $MgAl_2O_4$ spinel. Based on the results of transmission electron microscopy, most of the particles are determined to belong to a nanosized fraction with a size distribution from ~10 to ~200 nm. However, in the resulting material, there are a few particles in the submicron range of sizes.

An X-ray analysis of the thermal effect on the PDS product revealed the total completion of phase transitions during annealing at 1500°C. After annealing, the phase composition of the powder becomes stable and corresponds most accurately to the composition of α-Al_2O_3 and $MgAl_2O_4$.

Based on the results, we can conclude that the PDS product can be further used in the development of strong alumina ceramics with improved performance. Such improved ceramics can be used in various fields of science and technology, for example, for the manufacture of wear-resistant tools, heat loaded parts of gas turbines, and internal combustion engines. Owing to their special magnetic, dielectric, and optical properties, Al_2O_3-based ceramics are promising for the creation of high-temperature fuel cells, permanent magnets, microelectronics products with high density of elements, and nanomembrane.

REFERENCES

1. V. S. Kortov, A. E. Ermakov, A. F. Zatsepin, M. A. Uimin, S. V. Nikiforov, A. A. Mysik, and V. S. Gaviko, "Specific features of luminescence properties of nanostructured aluminum oxide," Phys. Solid State **50**, 957 (2008).
2. F. G. Lovshenko and G. F. Lovshenko, *Composite Nanostructured Mechanically Alloyed Powders for Gas-Thermal Coatings* (Belorus. Ros. Univ., Mogilev, 2013) [in Russian].
3. A. B. Vorozhtsov, M. Lerner, N. Rodkevich, H. Nie, A. Abraham, M. Schoenitz, and E. L. Drezin, "Oxidation of nano-sized aluminum powders," Thermochim. Acta **636**, 48–56 (2016).
4. N. F. Kosenko, "The reactivity of alumina vaterials," Ogneupory Tekh. Keram., Nos. 7–8, 3–15 (2010).
5. D. A. Zatsepin, V. M. Cherkashenko, E. Z. Kurmaev, S. N. Shamin, V. V. Fedorenko, N. A. Skorikov, S. V. Plastinin, N. V. Gavrilov, A. I. Medvedev, and S. O. Cholakh, "X-ray emission study of the electronic structure of nanocrystalline Al_2O_3," Phys. Solid State **46**, 2134 (2004).
6. S. P. Andriets, N. V. Dedov, E. M. Kutyavin, Yu. F. Ivanov, and E. V. Kozlov, "Structure and properties of plasma-chemical powders of aluminum oxide," Izv. Vyssh. Uchebn. Zaved., Tsvetn. Metall., No. 3, 64–70 (2008).
7. N. F. Kosenko, "Polymorphism of aluminum oxide," Vyssh. Uchebn. Zaved., Ser.: Khim. Khim. Tekhnol. **54** (5), 3–16 (2011).
8. A. V. Afanas'ev, V. A. Il'in, V. A. Moshnikov, E. N. Sokolova, and Yu. M. Spivak, "Synthesis of nanoand microporous structures by electrochemical methods," Biotekhnosfera, Nos. 1–2, 39–45 (2011).

9. J. Martin, M. Vazquez, M. Hernandez-Velez, and C. Mijangos, "One-dimensional magnetopolymeric nanostructures with tailored sizes," Nanotecnology **19**, 175304 (2008).

10. Yu. A. Kotov and V. V. Ivanov, "Powder nanotechnology for the creation of functional materials and devices for electrochemical power engineering," Vestn. Akad. Nauk **78**, 777–787 (2008).

11. C. J. Brinker and G. W. Scherer, *Sol-Gel Science: The Physics and Chemistry of Sol-Gel Processing* (Academic, New York, 2013).

12. V. A. Svetlichnyi, A. I. Stadnichenko, and I. N. Lapin, "Preparation of γ-$Al(OH)_3$ and γ-Al_2O_3 nanoparticles by the method of pulsed laser ablation of metal aluminum in water," Russ. Phys. J. **60**, 377 (2017).

13. A. A. Sivkov, A. A. Ivatushenko, O. B. Nazarenko, A. S. Saigash, A. Ya. Pak, and Yu. L. Kolganova, "Plasmodynamic synthesis of ultradisperse copper oxide in atmospheric conditions," Fiz. Khim. Obrab. Mater., No. 4, 25–34 (2015).

14. A. A. Sivkov, D. Yu. Gerasimov, and D. S. Nikitin, "Direct dynamic synthesis of nanodispersed phases of titanium oxides upon sputtering of electrodischarge titanium plasma into an air atmosphere," Tech. Phys. Lett. **43**, 16 (2017).

15. A. A. Evdokimov, "Plasmodynamic synthesis of ultradisperse titanium nitride and the production of TiN ceramics by the method of spark plasma sintering," Cand. Sci. (Tech. Sci.) Dissertation (2013).

16. A. I. Y. Tok, F. Y. C. Boey, and X. L. Zhao, "Novel synthesis of Al_2O_3 nano-particles by flame spray pyrolysis," J. Mater. Proc. Technol. **178**, 270–273 (2006).

17. F. B. Afruz and M. J. Tafreshi, "Synthesis of γ-Al_2O_3 nano particles by different combustion modes using ammonium carbonate," Indian J. Pure Appl. Phys. **52**, 378–385 (2014).

18. S. Hashimoto and A. Yamaguchi, "Synthesis of α-Al_2O_3 platelets using sodium sulfate flux," J. Mater. Res. **14**, 4667–4672 (1999).

Translated by A. Ivanov